Raman scattering in the transition-metal dichalcogenides of $1T'$-$MoTe_2$, T_d-$MoTe_2$, and T_d-WTe_2

Xiaoli Ma,[1] Pengjie Guo,[1] Changjiang Yi,[2] Qiaohe Yu,[1] Anmin Zhang,[1] Jianting Ji,[1] Yong Tian,[1] Feng Jin,[1] Yiyan Wang,[1] Kai Liu,[1] Tianlong Xia,[1] Youguo Shi,[2] and Qingming Zhang[1,3,*]

[1]*Department of Physics, Beijing Key Laboratory of Opto-Electronic Functional Materials and Micro-Nano Devices, Renmin University of China, Beijing 100872, People's Republic of China*

[2]*Beijing National Laboratory for Condensed Matter Physics, Institute of Physics, Chinese Academy of Sciences, Beijing 100190, People's Republic of China*

[3]*Department of Physics and Astronomy, Shanghai Jiao Tong University, Shanghai 200240 and Collaborative Innovation Center of Advanced Microstructures, Nanjing 210093, People's Republic of China*

(Received 13 September 2016; revised manuscript received 11 November 2016; published 13 December 2016)

We comparably performed polarized Raman scattering studies of $MoTe_2$ and WTe_2. By rotating crystals to tune the angle between the principal axis of the crystals and the polarization of the incident/scattered light, we obtained the angle dependence of the intensities for all the observed modes, which is perfectly consistent with careful symmetry analysis. Combining these results with first-principles calculations, we clearly identified the observed phonon modes in the different phases of both crystals. Fifteen Raman-active phonon modes ($10\,A_g + 5\,B_g$) in the high-symmetry phase $1T'$-$MoTe_2$ (300 K) were well assigned, and all the symmetry-allowed Raman modes ($11\,A_1 + 6\,A_2$) in the low-symmetry phase T_d-$MoTe_2$ (10 K) and 12 Raman phonons ($8\,A_1 + 4\,A_2$) in T_d-WTe_2 were observed and identified. The present paper provides basic information about the lattice dynamics in transition-metal dichalcogenides and may shed some light on the understanding of the extremely large magnetoresistance in this class of materials.

DOI: 10.1103/PhysRevB.94.214105

I. INTRODUCTION

Both $MoTe_2$ and WTe_2 are nonmagnetic thermoelectric semimetals [1,2] discovered in the mid-twentieth century. They have recently attracted a great deal of interest in the fields of condensed matter physics and materials science because of the extremely large magnetoresistance (MR) found in this class of nonmagnetic compounds [3–10]. In T_d-WTe_2, for example, a huge MR at low temperatures is observed when a magnetic field and current are applied along the c axis and the a axis, respectively. At 0.53 K, the MR under a 60 T field can reach $1.3 \times 10^7\%$ with no saturation trend. Ali *et al.* found that the electron pocket is essentially the same size as the hole pocket [3] at low temperatures in T_d-WTe_2. This has been experimentally verified using a variety of methods, including angle-resolved photoemission spectroscopy (ARPES) [11–13], quantum oscillation [14,15], and Hall effect [16] experiments. Experiments performed under high pressure have indicated that the difference between electron and hole pockets increases with increasing pressure, at the same time MR is gradually suppressed [14]. Therefore, the origin of the huge MR may be attributable to the perfect compensation of electrons and hole pockets [3,11,14,15,17]. In fact, the mechanism of the extremely large MR remains an open question. In addition, superconducting transition has been observed in T_d-$MoTe_2$ and T_d-WTe_2 under pressure [18–20]. For T_d-WTe_2, T_c can reach 7 K under a pressure of 16.8 GPa [18], and T_c goes up to 8.2 K at $P = 11.7$ GPa in T_d-$MoTe_2$ [20]. Interestingly, very recent studies show that T_d-$MoTe_2$ and T_d-WTe_2 are Type-II Weyl semimetals with a layered structure [21,22], whose Weyl point exists at the interface of electron and hole pockets. In fact, most other layered transition-metal dichalcogenides (TMDs), including MoS_2 [23–27] and WSe_2 [28–31], are semiconductors, which are directly related to their different structures.

Generally, TMDs can assume various configurations, including the $2H$, $1T$, $1T'$, and T_d structures. $MoTe_2$ can exist in the $2H$ (hexagonal, space group $P6_3/mmc$), $1T'$ (monoclinic, space group $P2_1/m$), or T_d structure (orthorhombic structure, space group $Pnm2_1$) [32]. The $1T'$ and T_d structures are quite similar, and both of them have a half-metallic state [10,22]. The symmetry change between the two structures originates from dislocations between stacked layers [22,33]. With decreasing temperature, a structural transition occurs in $MoTe_2$ from the monoclinic $1T'$ phase to the orthogonal T_d phase at $\sim$270 K, and it is reported that the transition is the first-order one [34]. The T_d structure of $MoTe_2$ is isomorphic with the T_d structure of WTe_2, and both of them exhibit a huge MR effect. WTe_2, a layered compound with a half-metallic state [1,3,35,36], usually has a stable T_d structure (crystallized into an orthogonal structure of distorted octahedra at atmospheric pressure, space group $Pnm2_1$) [37]. By contrast, many other TMDs are usually semiconductors with $2H$ or $1T$ structures. $MoTe_2/WTe_2$ and other TMD materials have lately attracted widespread attention because of their rich physics, such as their huge MR effect, superconducting transition under pressure, and Weyl semimetal states, among other phenomena.

Raman scattering is among the most conventional and fundamental techniques for studying TMDs. It can determine the structure and layer number in an easy and nondestructive manner [38–42]. Studies of the lattice dynamics of these materials lay the foundation for exploring possible lattice structures and the influence of phonons on electronic energy bands. It is provides an important basis for the study of $MoTe_2$ and WTe_2 heterojunctions and their doping and phase transitions [2,43–45].

*qmzhang@ruc.edu.cn

In this paper, we conducted a systematic Raman study of $MoTe_2$ and WTe_2. Fifteen Raman-active modes ($10\ A_g + 5\ B_g$) were measured in $1T'$-$MoTe_2$. All $17\ A_1/A_2$ Raman modes ($11\ A_1 + 6\ A_2$) in T_d-$MoTe_2$ and 12 Raman modes ($8\ A_1 + 4\ A_2$) in T_d-WTe_2 were observed. To resolve the observed phonon modes in $MoTe_2$ and WTe_2, we performed polarized Raman measurements. The mode intensity modulations induced by rotating the samples confirmed their symmetries, which are in good agreement with strict symmetry analysis. We further conducted first-principles calculations. Combining symmetry analysis with first-principles calculations allowed us to clearly identify all the observed modes. The corresponding vibration patterns were also given.

II. EXPERIMENTAL METHOD

Single crystals of $MTe_2(M = \mathrm{Mo, W})$ were grown by a flux method, as described in the literature [14]. T_d-$MoTe_2$ and $1T'$-$MoTe_2$ are the low-T (10 K) and high-T (300 K) phases of the same crystal measured at different temperature. The polarized and angular Raman spectra were collected using a HR800 spectrometer (Jobin Yvon) equipped with a liquid-nitrogen-cooled charge-coupled device (CCD) and volume Bragg gratings, for which micro-Raman backscattering configuration was adopted. A 633 nm laser was used, with a spot size of $\sim 5\,\mu$m focused on the sample surface. The laser power was maintained at approximately 1.4 mW to avoid overheating during measurements.

The X,Y in this paper correspond to the a,b axis of crystalline $MTe_2\,(M = \mathrm{Mo, W})$ respectively. The X',Y' is a 45° angle with respect to X,Y. The Z is perpendicular to the XY plane. The angle dependence of the mode intensity was measured by rotating the crystals, while the polarizations of the incident and scattered light were fixed. In principle, rotating the crystals gives the same consequences as rotating the locked incident and scattered light polarizations because the aim of both operations is to change the angle between the polarizations of the incident light and the principal axes. The Raman tensors determine the intensity modulations with the angle; however, rotating the sample is technically more advantageous. The reason is that changing the polarization of incident light needs at least two more polarizers in the incident and scattered light path and a careful adjustment of their angle matching. Usually it is relatively inaccurate compared to the simple sample rotation, and the outer light path consisting of many optical pieces always has a polarization dependence of efficiency and is not easy to be compensated. This will bring further inaccuracy to Raman intensities if changing the polarizations. To obtain more accurate and consistent data, we chose to rotate the crystals rather than to change light polarizations in the present paper.

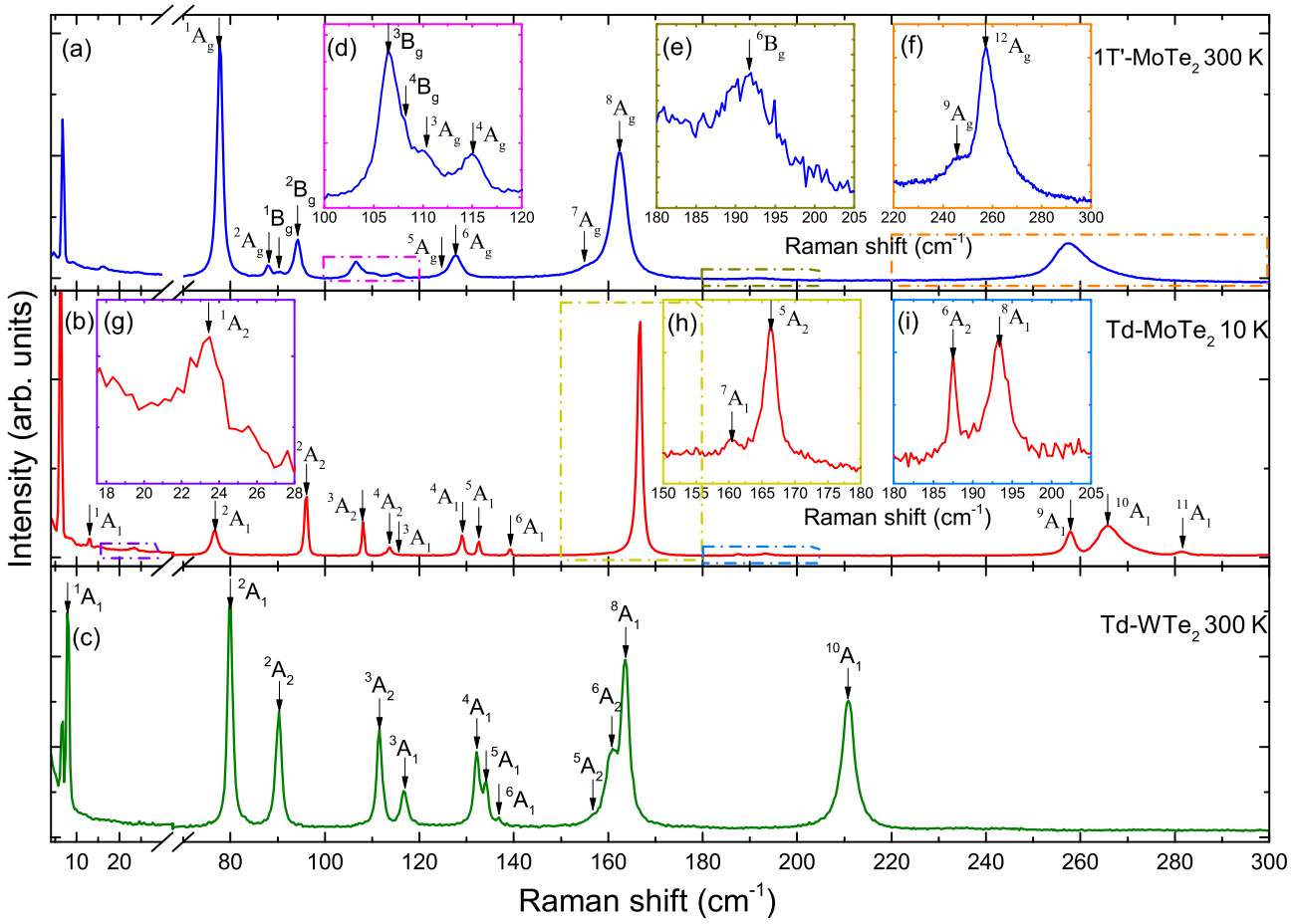

FIG. 1. (a) Raman spectrum of $1T'$-$MoTe_2$ measured at 300 K; (d)–(f) are enlarged to show the modes with weak intensities in (a). (b) Raman spectrum of T_d-$MoTe_2$ measured at 10 K; (g)–(i) are enlarged to show the modes with weak intensities in (b). T_d-$MoTe_2$ and $1T'$-$MoTe_2$ are the low T and high T phases of the same sample, respectively. (c) Raman spectrum of T_d-WTe_2 measured at 300 K.

III. CALCULATION METHOD

To determine the phonon modes of WTe_2 and $MoTe_2$, we conducted first-principles electronic structure calculations using the projector-augmented wave method [46], as implemented in the Vienna Ab initio Simulation Package (VASP) package [47]. For the exchange-correlation potential, the generalized gradient approximation (GGA) of Perdew-Burke-Ernzerhof [48] was adopted. To describe the van der Waals (vdW) interaction in layered systems not included in conventional density functional theory, the vdW-optB86b function [49] was chosen. The kinetic energy cutoff of the plane-wave basis was set to 300 eV. The simulations were performed with an orthorhombic supercell containing 4 W atoms and 8 Te atoms. A $20 \times 10 \times 8$ k-point mesh was employed for the Brillouin zone sampling. Gaussian smearing with a width of 0.01 eV was used around the Fermi surface. In the structure optimization, both the cell parameters and internal atomic positions were allowed to relax until all forces were smaller than 0.005 eV/Å. The calculated lattice parameters were in good agreement with the experimental values (error less than 1.7%) [33]. After the equilibrium structure was obtained, the vibrational frequencies and polarization vectors at the Brillouin zone center were calculated using the dynamic matrix method.

IV. RESULTS AND DISCUSSIONS

Figure 1(a) shows the Raman spectrum of $1T'$-$MoTe_2$ collected at 300 K. $1T'$-$MoTe_2$ has a monoclinic structure with space group $P2_1/m(C_{2h})$ [32,37], which allows 18 Raman-active phonon modes (12 A_g modes and 6 B_g modes). These modes should be visible when the incident light vertically strikes the ab plane. In fact, we observed 15 Raman-active phonon modes. The other three modes are invisible, perhaps due to weak signals. The signal at the lowest frequencies arises from the laser line.

Figures 1(b) and 1(c) show the spectrum of T_d-$MoTe_2$ measured at 10 K and the spectrum of T_d-WTe_2 measured at 300 K, respectively. T_d-$MoTe_2$ and T_d-WTe_2 have the same orthorhombic structure with space group $Pnm2_1(C_{2v}^7)$ [50]. Symmetry analysis indicates that there should be 33 Raman-

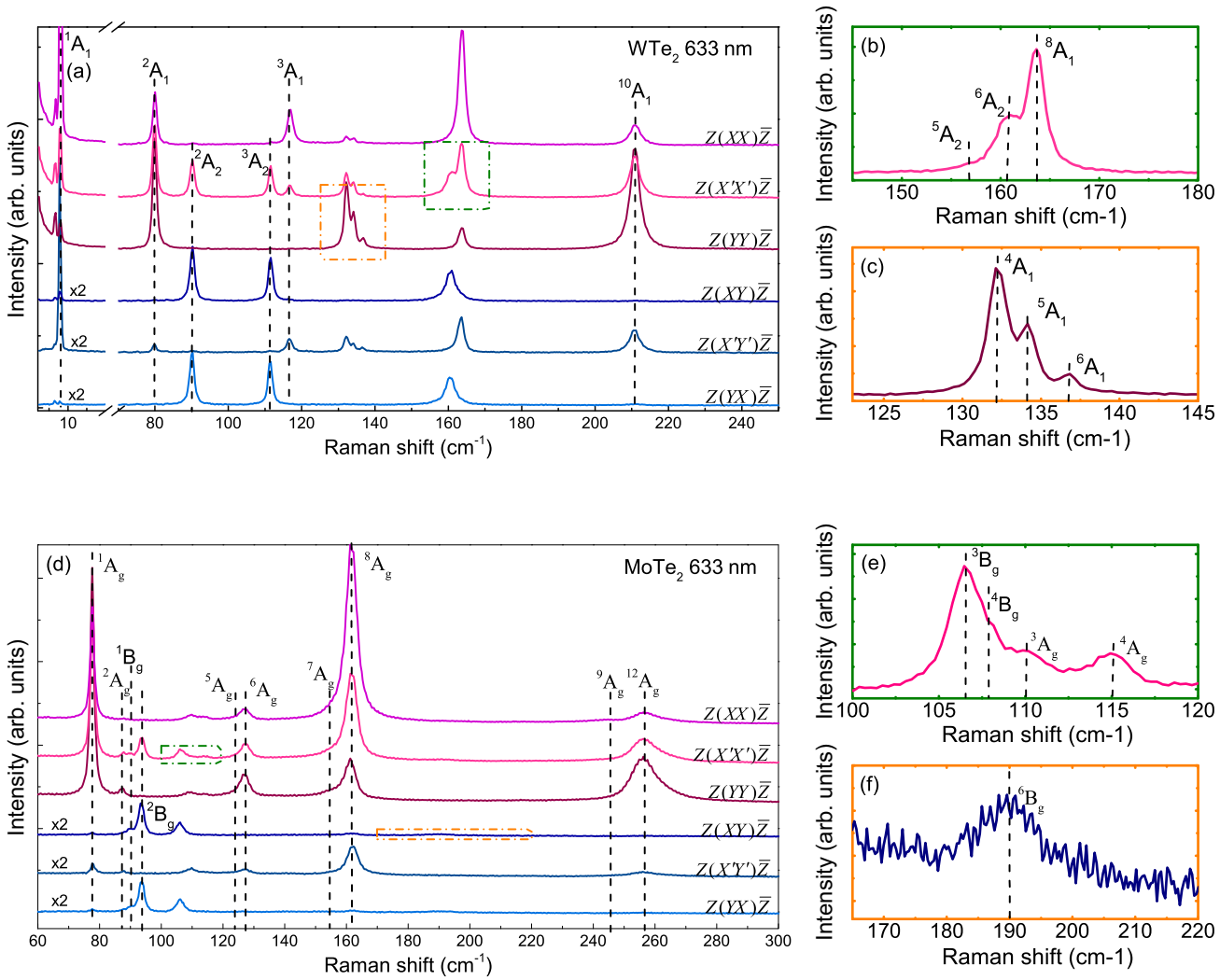

FIG. 2. (a) Polarized Raman spectrum of T_d-WTe_2 collected at room temperature using a 633 nm laser. (b), (c) Zoomed-in views of the green/orange-dotted box in (a). (d) Polarized Raman spectrum of $1T'$-$MoTe_2$ collected at room temperature using a 633 nm laser. (e), (f) Zoomed-in views of the green/orange-dotted box in (d).

active phonon modes [11 $A_1 + 6\ A_2 + 5\ B_1 + 11\ B_2$] in the low-symmetry phase. Our measurements were conducted on the ab plane, which allows 17 Raman modes (11 $A_1 + 6\ A_2$). All 17 modes were observed in the spectrum of T_d-$MoTe_2$. By comparison, only 12 Raman modes were observed in the spectrum of T_d-WTe_2 under the same experimental conditions. The reason for this difference may be weak signals of the other five phonon modes. As in the spectrum of $1T'$-$MoTe_2$ [Fig. 1(a)], the peak at the lowest frequencies in the spectrum of T_d-$MoTe_2$ [Fig. 1(b)] originates from the excitation laser spectrum; by contrast, the peaks at the lowest frequencies in the spectrum of T_d-WTe_2 [Fig. 1(c)] actually contain a phonon mode in addition to the laser line. Raman spectra of $1T'$- and T_d-$MoTe_2$ look a little different, while some similarity can still be seen because of the structural inheritance between the two phases [Figs. 1(a) and 1(b)]. Hexagonal 2H-$MoTe_2$, however, has a higher lattice symmetry, much different from $1T'$- and T_d-$MoTe_2$. That is why fewer Raman bands can be observed in the $2H$ phase [51,52]. To verify the symmetry of the observed modes, we collected the corresponding polarized Raman spectra.

Figure 2 shows the polarized Raman spectra of T_d-WTe_2 and $1T'$-$MoTe_2$ at room temperature under different polarization configurations. Totals of 12 and 15 Raman modes can be seen in the spectra of T_d-WTe_2 and $1T'$-$MoTe_2$, respectively. Comparison of the spectra of the two similar structures demonstrates that the subtle structural difference is clearly distinguished by Raman scattering.

Bulk T_d-WTe_2 has an orthogonal structure with the space group $Pnm2_1(C_{2v}^7)$ [50], in which layers are stacked along the c axis. Generally, Raman intensities are determined by Raman tensors. The Raman tensors for WTe_2 are as follows:

$$A_1 = \begin{pmatrix} a & 0 & 0 \\ 0 & b & 0 \\ 0 & 0 & c \end{pmatrix}, \quad A_2 = \begin{pmatrix} 0 & d & 0 \\ d & 0 & 0 \\ 0 & 0 & 0 \end{pmatrix},$$

$$B_1 = \begin{pmatrix} 0 & 0 & e \\ 0 & 0 & 0 \\ e & 0 & 0 \end{pmatrix}, \quad B_2 = \begin{pmatrix} 0 & 0 & 0 \\ 0 & 0 & f \\ 0 & f & 0 \end{pmatrix}.$$

Symmetry analysis indicates that only the A_1 and A_2 modes are visible in our case because our measurements were conducted on the ab plane. According to the tensors of the A_1 and A_2 modes, all 12 Raman modes can be seen in the channel of $Z(X'X')\bar{Z}\,(e_i \parallel e_s, \theta = 45°)$ or $Z(X'Y')\bar{Z}\,(e_i \perp e_s, \theta = 45°)$; by contrast, in $Z(XX)\bar{Z}\,(e_i \parallel e_s, \theta = 0°)$ or $Z(YY)\bar{Z}\,(e_i \parallel e_s, \theta = 90°)$, only eight A_1 modes should be observed. Experimentally, these modes are located at 8.0 cm^{-1} ($^1A_1$), 80.1 cm^{-1}

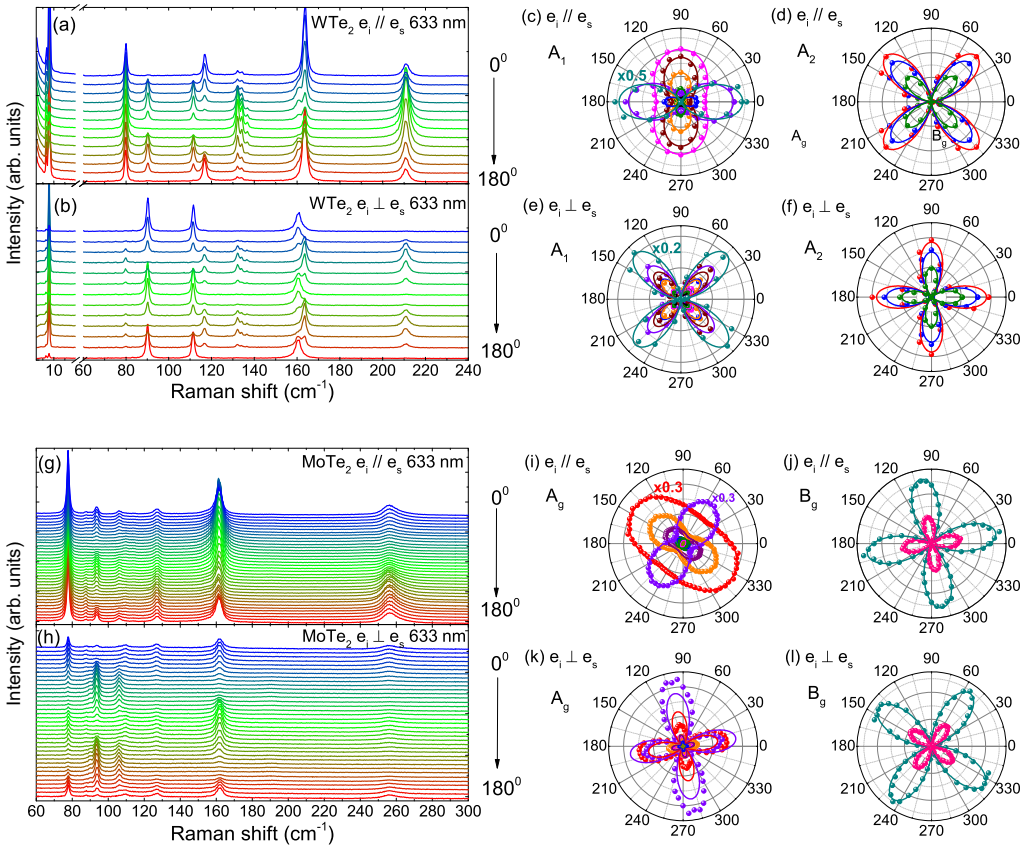

FIG. 3. (a), (b) Angle dependence of T_d-WTe_2 in parallel and cross-polarization configurations. (g), (h) Angle dependence of $1T'$-$MoTe_2$ in parallel and cross-polarization configurations. (c)–(f) Intensity plots with respect to rotation angle for the A_1/A_2 modes of T_d-WTe_2. (i)–(l) Intensity plots with respect to rotation angle for the A_g/B_g modes of $1T'$-$MoTe_2$.

($^2A_1$), 117.7 cm^{-1} ($^3A_1$), 132.9 cm^{-1} ($^4A_1$), 134.8 cm^{-1} ($^5A_1$), 138.4 cm^{-1} ($^6A_1$), 164.5 cm^{-1} ($^8A_1$), and 212.0 cm^{-1} ($^9A_1$). In the case of $Z(XY)\bar{Z}$ ($e_i \perp e_s, \theta = 0^\circ$) or $Z(YX)\bar{Z}$ ($e_i \perp e_s, \theta = 90^\circ$), only four A_2 modes are visible, located at 90.6 cm^{-1} ($^2A_2$), 112.1 cm^{-1} ($^3A_2$), 156.1 cm^{-1} ($^5A_2$), and 161.2 cm^{-1} ($^6A_2$). Through careful polarized Raman measurements, we can easily distinguish the A_1 and A_2 modes.

Bulk $1T'$-$MoTe_2$ has a monoclinic structure with the space group $P2_1/m(C_{2h})$ [32,37]. Its Raman tensors are written as follows:

$$A_g = \begin{pmatrix} b & 0 & d \\ 0 & c & 0 \\ d & 0 & a \end{pmatrix}, \quad B_g = \begin{pmatrix} 0 & f & 0 \\ f & 0 & e \\ 0 & e & 0 \end{pmatrix}.$$

Symmetry analysis tells us that the A_g and B_g modes are visible when the measurements are conducted on the ab plane. The tensors of the A_g and B_g modes allow 15 Raman modes in $Z(X'X')\bar{Z}$ ($e_i \parallel e_s, \theta = 45^\circ$) or $Z(X'Y')\bar{Z}$ ($e_i \perp e_s, \theta = 45^\circ$), and all of them were observed in this paper. Only 10 A_g modes are observed in $Z(XX)\bar{Z}$ ($e_i \parallel e_s, \theta = 0^\circ$) or $Z(YY)\bar{Z}$ ($e_i \parallel e_s, \theta = 90^\circ$). Experimentally, these modes correspond to 77.0 cm^{-1} (^1A_g), 86.3 cm^{-1} (^2A_g), 110.7 cm^{-1} (^3A_g), 114.5 cm^{-1} (^4A_g), 127.8 cm^{-1} (^5A_g), 129.0 cm^{-1} (^6A_g), 155.4 cm^{-1} (^7A_g), 163.3 cm^{-1} (^8A_g), 245.0 cm^{-1} (^9A_g), and 256.3 cm^{-1} ($^{12}A_g$). In $Z(XY)\bar{Z}$ ($e_i \perp e_s, \theta = 0^\circ$) or $Z(YX)\bar{Z}$ ($e_i \perp e_s, \theta = 90^\circ$), only five B_g modes should be observed, corresponding to 91.2 cm^{-1} (^1B_g), 94.4 cm^{-1} (^2B_g), 106.1 cm^{-1} (^3B_g), 107.0 cm^{-1} (^4B_g), and 191.2 cm^{-1} (^6B_g). Thus, the A_g or B_g modes can be distinguished through different polarization configurations.

Figures 3(a), 3(b), 3(g), and 3(h) show the angle dependence of the Raman intensities for T_d-WTe_2/$1T'$-$MoTe_2$ in both parallel and cross channels, demonstrating that the Raman intensities exhibit a regular change as the crystals are rotated. The intensity variations are illustratively summarized in Figs. 3(c)–3(f) and 3(i)–3(l). Here, e_i and e_s are the polarizations of the incident and scattered light, respectively. The angle between the polarizations of the incident light and the principal axis (axis a) is defined as θ.

According to the aforementioned Raman tensors, the Raman intensities for different symmetries in T_d-WTe_2 can

TABLE I. Comparison of the calculated and experimental optical phonon modes (in cm^{-1}) for T_d-$MoTe_2$/T_d-WTe_2 and $1T'$-$MoTe_2$. The main atomic motions of the modes are also given (see Fig. 4). I and R denote infrared and Raman activities, respectively.

T_d-$MoTe_2$/T_d-WTe_2				$1T'$-$MoTe_2$			
Symmetry	Calculation	Experiment	Activity	Symmetry	Calculation	Experiment	Activity
$^1A_1$	10.3/9.5	13.0/8.0	I + R	^1B_u	8.8		I
$^1A_2$	26.9/24.3	23.6	R	^1A_u	26.3		I
$^1B_2$	32.1/28.2		I + R	^2B_u	32.5		I
$^2A_1$	77.4/76.2	76.7/80.1	I + R	^1A_g	76.6	77.0	R
$^2B_2$	85.8/86.1		I + R	^2A_g	84.8	86.3	R
$^1B_1$	88.5/87.1		I + R	^1B_g	88.2	91.2	R
$^2A_2$	91.2/88.1	96.1/90.6	R	^2B_g	91.0	94.4	R
$^3A_2$	104.6/109.7	108.1/112.1	R	^3B_g	104.0	106.1	R
$^2B_1$	105.3/110.0		I + R	^4B_g	104.7	107.0	R
$^4A_2$	108.0/113.0	113.7	R	^2A_u	107.9		I
$^3A_1$	108.7/113.2	115.5/117.7	I + R	^3A_g	109.4	110.7	R
$^3B_1$	110.6/115.2		I + R	^3A_u	110.4		I
$^3B_2$	113.0/117.6		I + R	^4A_g	113.6	114.5	R
$^4B_2$	115.1/123.0		I + R	^3B_u	116.0		I
$^4A_1$	122.4/128.5	129.1/132.9	I + R	^4B_u	123.4		I
$^5A_1$	125.1/130.6	132.6/134.8	I + R	^5A_g	125.5	127.8	R
$^5B_2$	127.3/132.3		I + R	^6A_g	127.0	129.0	R
$^6B_2$	128.9/127.4		I + R	^5B_u	129.0		I
$^6A_1$	134.2/132.0	139.2/138.4	I + R	^6B_u	133.9		I
$^7B_2$	153.7/154.8		I + R	^7A_g	153.2	155.4	R
$^7A_1$	158.6/158.8	160.4	I + R	^8A_g	158.5	163.3	R
$^5A_2$	175.9/151.0	166.7/156.1	R	^4A_u	175.5		I
$^4B_1$	176.3/151.2		I + R	^5A_u	176.2		I
$^6A_2$	188.4/159.5	187.5/161.2	R	^5B_g	186.9		R
$^5B_1$	188.9/161.0		I + R	^6B_g	187.9	191.2	R
$^8A_1$	191.2/171.9	193.3/164.5	I + R	^7B_u	190.8		I
$^8B_2$	191.4/170.7		I + R	^8B_u	191.6		I
$^9A_1$	244.9/209.1	258.1/212.0	I + R	^9A_g	242.0	245.0	R
$^9B_2$	245.6/210.6		I + R	$^{10}A_g$	246.8		R
$^{10}B_2$	251.6/205.8		I + R	$^{11}A_g$	252.4		R
$^{10}A_1$	251.6/205.6	265.4	I + R	$^{12}A_g$	254.9	256.3	R
$^{11}B_2$	265.1/231.7		I + R	^9B_u	266.6		I
$^{11}A_1$	265.9/231.2	280.4	I + R	$^{10}B_u$	267.3		I

be written as follows:

$$e_i \parallel e_s : A_1 : I = [b + (a - b)\cos^2\theta]^2, \quad (1)$$

$$A_2 : I = (d \sin 2\theta)^2, \quad (2)$$

$$e_i \perp e_s : A_1 : I = \left(\frac{b - a}{2} \sin 2\theta\right)^2, \quad (3)$$

$$A_2 : I = (d \cos 2\theta)^2. \quad (4)$$

Similarly, the Raman intensities for the different symmetries in $1T'$-$MoTe_2$ have the following forms:

$$e_i \parallel e_s : A_g : I = [c + (b - c)\cos^2\theta]^2, \quad (5)$$

$$B_g : I = (f \sin 2\theta)^2, \quad (6)$$

$$e_i \perp e_s : A_g : I = \left(\frac{c - b}{2} \sin 2\theta\right)^2, \quad (7)$$

$$B_g : I = (f \cos 2\theta)^2. \quad (8)$$

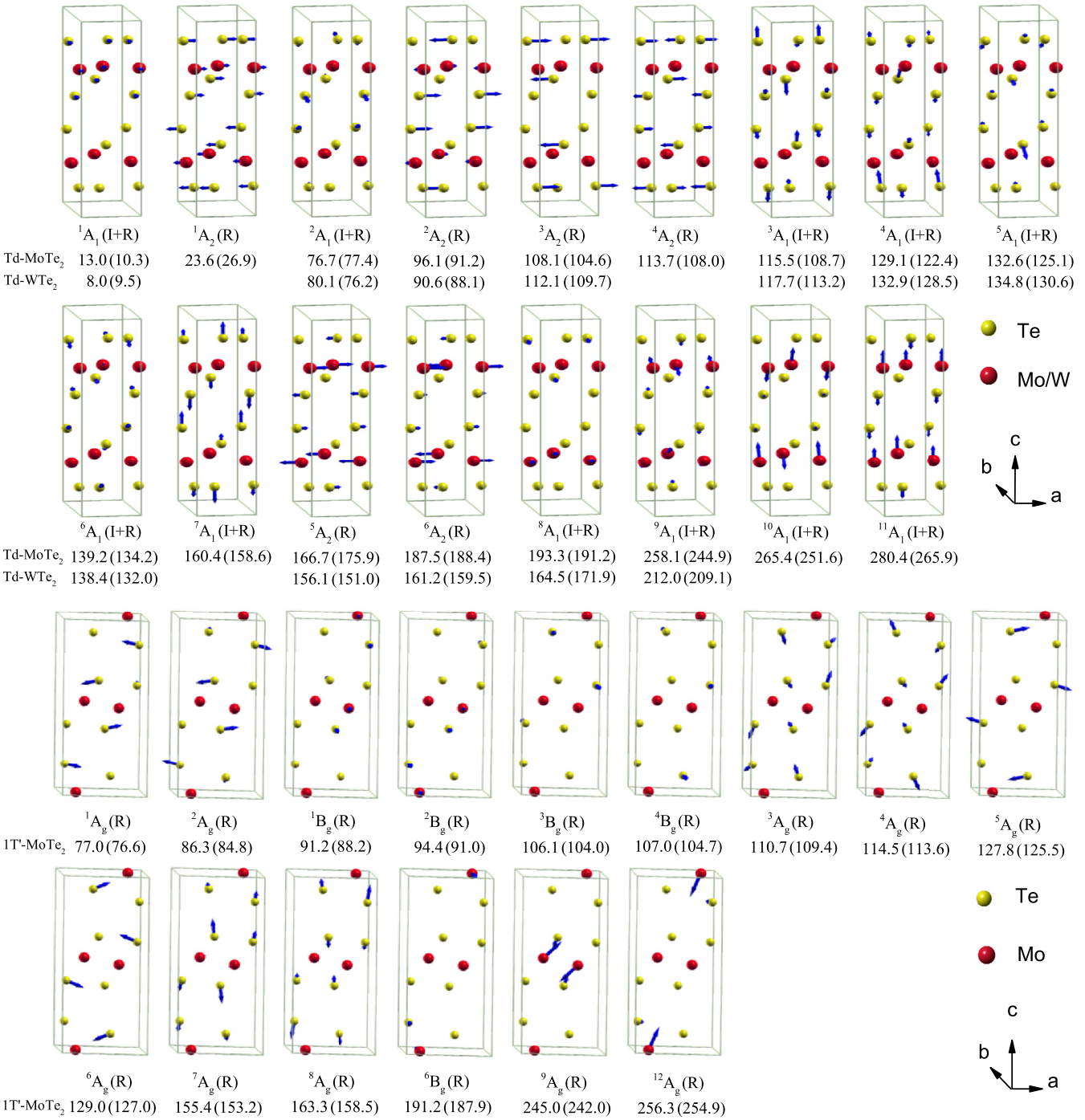

FIG. 4. Vibration patterns of all the Raman modes observed in T_d-$MoTe_2$/T_d-WTe_2 and $1T'$-$MoTe_2$. The mode symmetry, optical activity, and experimental (calculated) phonon frequency are also listed below each pattern. I/R indicates infrared/Raman activity.

Although the two structures are similar, polarized Raman measurements can reveal subtle dependencies. The angle dependence for the $A_1(A_g)$ modes in the parallel channel exhibits twofold symmetry, whereas the angle dependence for the $A_2(B_g)$ modes exhibits fourfold symmetry. The angle dependence for the A_1/A_2 and A_g/B_g modes in the cross channel exhibits fourfold symmetry; however, the maximum intensities appear at different angles depending on the mode symmetries. Notably, the nonzero starting angle of $1T'$-$MoTe_2$ has been taken into account. Figures 3(c)–3(f) and 3(i)–3(l) indicate that the detailed symmetry analysis shows good consistency with the experimental results. This consistency indicates that the symmetry identification for each phonon in T_d-WTe_2 and $1T'$-$MoTe_2$ is reasonable.

To assign the observed modes, we conducted first-principles calculations. The experimental and calculated mode frequencies are summarized in Table I. The table indicates that the experimental values agree well with the calculated data. In total, there are 11 $A_1 + 6$ $A_2 + 5$ $B_1 + 11$ B_2 vibration modes in T_d-$MoTe_2$/T_d-WTe_2. Among them, six A_2 modes are Raman active, and the rest are infrared and Raman active. A total of 12 $A_g + 6$ $B_g + 5$ $A_u + 10$ B_u vibration modes are allowed in $1T'$-$MoTe_2$. Of these modes, 12 A_g modes and six B_g modes are Raman active, and the remaining five A_u modes and 10 B_u modes are infrared active.

The vibration patterns of the observed phonon modes are illustrated in Fig. 4. T_d-WTe_2 and T_d-$MoTe_2$ have the same structure and identical vibration patterns. The first two rows of Fig. 4 show the vibration patterns of T_d-WTe_2 and T_d-$MoTe_2$. Because the effective mass m of W is larger than that of Mo and because $\omega \propto \sqrt{k/m}$, the phonon frequency ω of T_d-WTe_2 is expected to be smaller than that of T_d-$MoTe_2$ for the same mode. The calculations indicate that most of the modes follow this expectation; however, a few phonon modes appear anomalous, which may be due to the change in the relevant spring constants. Meanwhile, the experimental data are consistent with the calculations, which supports the previous speculation concerning ω. The last two rows of Fig. 4 show the vibration patterns of $1T'$-$MoTe_2$. The phase transition from the $1T'$ phase to the T_d phase in $MoTe_2$ is correlated with the stacked misalignment between the layers. A comparison between the interlayer modes of $1T'$-$MoTe_2$ (e.g., ${}^7A_g$) and the interlayer modes of T_d-$MoTe_2$ (e.g., ${}^7A_1$) reveals that the corresponding vibration patterns show only small changes across the phase transition. This result suggests that the phase transition has little effect on the interlayer modes.

V. CONCLUSION

This paper gives a comprehensive identification of the vibration modes for $1T'$-$MoTe_2$, T_d-$MoTe_2$, and T_d-WTe_2. The polarized Raman spectra of bulk $1T'$-$MoTe_2$, T_d-$MoTe_2$, and T_d-WTe_2 were collected, and 15, 17, and 12 Raman-active phonon modes were observed, respectively. The $A_1(A_g)$ and $A_2(B_g)$ modes were distinguished by careful polarized measurements combined with group-theory analysis. First-principles calculations were conducted to identify the vibration pattern for each mode. Comparison of the vibration patterns of the interlayer modes of $1T'$-$MoTe_2$ and T_d-$MoTe_2$ revealed that the phase transition has very little influence on the interlayer modes. These results may have important implications for studies of $MoTe_2$ and WTe_2 heterojunctions, doping, and phase transitions, among other topics.

ACKNOWLEDGMENTS

This paper was supported by the Ministry of Science and Technology of China (Grant No. 2016YFA0300504) and the National Science Foundation of China. Y.G.S was supported by the Strategic Priority Research Program (B) of the Chinese Academy of Sciences (Grant No. XDB07020100). Q.M.Z., A.M.Z., K.L., and T.L.X were supported by the Fundamental Research Funds for the Central Universities and the Research Funds of Renmin University of China (Grants No. 10XNI038, No. 14XNLF06, No. 14XNLQ03, and No. 14XNLQ07). Computational resources were provided by the Physical Laboratory of High Performance Computing at Renmin University of China. The atomic structures and vibrational displacement patterns were prepared using the XCRYSDEN program [53].

[1] S. Kabashima, J. Phys. Soc. Jpn. **21**, 945 (1966).
[2] E. Revolinsky, J. Appl. Phys. **35**, 2086 (1964).
[3] M. N. Ali, J. Xiong, S. Flynn, J. Tao, Q. D. Gibson, L. M. Schoop, T. Liang, N. Haldolaarachchige, M. Hirschberger, N. P. Ong, and R. J. Cava, Nature **514**, 205 (2014).
[4] T. Liang, Q. Gibson, M. N. Ali, M. H. Liu, R. J. Cava, and N. P. Ong, Nat. Mater. **14**, 280 (2015).
[5] E. Mun, H. Ko, G. J. Miller, G. D. Samolyuk, S. L. Bud'ko, and P. C. Canfield, Phys. Rev. B **85**, 035135 (2012).
[6] K. F. Wang, D. Graf, L. J. Li, L. M. Wang, and C. Petrovic, Sci. Rep. **4**, 7328 (2014).
[7] C. Zhang, Z. Yuan, S. Xu, Z. Lin, B. Tong, M. Z. Hasan, J. Wang, C. Zhang, and S. Jia, arXiv:1502.00251.
[8] P. B. Alers and R. T. Webber, Phys. Rev. **91**, 1060 (1953).
[9] C. Shekhar, A. K. Nayak, Y. Sun, M. Schmidt, M. Nicklas, I. Leermakers, U. Zeitler, Y. Skourski, J. Wosnitza, Z. K. Liu, Y. L. Chen, W. Schnelle, H. Borrmann, Y. Grin, C. Felser, and B. H. Yan, Nat. Phys. **11**, 645 (2015).
[10] D. H. Keum, S. Cho, J. H. Kim, D. H. Choe, H. J. Sung, M. Kan, H. Kang, J. Y. Hwang, S. W. Kim, H. Yang, K. J. Chang, and Y. H. Lee, Nat. Phys. **11**, 482 (2015).
[11] I. Pletikosic, M. N. Ali, A. V. Fedorov, R. J. Cava, and T. Valla, Phys. Rev. Lett. **113**, 216601 (2014).
[12] J. Jiang, F. Tang, X. C. Pan, H. M. Liu, X. H. Niu, Y. X. Wang, D. F. Xu, H. F. Yang, B. P. Xie, F. Q. Song, P. Dudin, T. K. Kim, M. Hoesch, P. K. Das, I. Vobornik, X. G. Wan, and D. L. Feng, Phys. Rev. Lett. **115**, 166601 (2015).
[13] Y. Wu, N. H. Jo, M. Ochi, L. Huang, D. X. Mou, S. L. Bud'ko, P. C. Canfield, N. Trivedi, R. Arita, and A. Kaminski, Phys. Rev. Lett. **115**, 166602 (2015).
[14] P. L. Cai, J. Hu, L. P. He, J. Pan, X. C. Hong, Z. Zhang, J. Zhang, J. Wei, Z. Q. Mao, and S. Y. Li, Phys. Rev. Lett. **115**, 057202 (2015).

[15] Z. W. Zhu, X. Lin, J. Liu, B. Fauque, Q. Tao, C. L. Yang, Y. G. Shi, and K. Behnia, Phys. Rev. Lett. **114**, 176601 (2015).
[16] Y. K. Luo, H. Li, Y. M. Dai, H. Miao, Y. G. Shi, H. Ding, A. J. Taylor, D. A. Yarotski, R. P. Prasankumar, and J. D. Thompson, Appl. Phys. Lett. **107**, 182411 (2015).
[17] H. Y. Lv, W. J. Lu, D. F. Shao, Y. Liu, S. G. Tan, and Y. P. Sun, Europhys. Lett. **110**, 37004 (2015).
[18] X. C. Pan, X. L. Chen, H. M. Liu, Y. Q. Feng, Z. X. Wei, Y. H. Zhou, Z. H. Chi, L. Pi, F. Yen, F. Q. Song, X. G. Wan, Z. R. Yang, B. G. Wang, G. H. Wang, and Y. H. Zhang, Nat. Commun. **6**, 7805 (2015).
[19] D. F. Kang, Y. Z. Zhou, W. Yi, C. L. Yang, J. Guo, Y. G. Shi, S. Zhang, Z. Wang, C. Zhang, S. Jiang, A. G. Li, K. Yang, Q. Wu, G. M. Zhang, L. L. Sun, and Z. X. Zhao, Nat. Commun. **6**, 7804 (2015).
[20] Y. P. Qi, P. G. Naumov, M. N. Ali, C. R. Rajamathi, W. Schnelle, O. Barkalov, M. Hanfland, S. C. Wu, C. Shekhar, Y. Sun, V. Süß, M. Schmidt, U. Schwarz, E. Pippel, P. Werner, R. Hillebrand, T. Förster, E. Kampert, S. Parkin, R. J. Cava *et al.*, Nat. Commun. **7**, 11038 (2016).
[21] A. A. Soluyanov, D. Gresch, Z. Wang, Q. Wu, M. Troyer, X. Dai, and B. A. Bernevig, Nature **527**, 495 (2015).
[22] Y. Sun, S. C. Wu, M. N. Ali, C. Felser, and B. H. Yan, Phys. Rev. B **92**, 161107 (2015).
[23] K. F. Mak, C. Lee, J. Hone, J. Shan, and T. F. Heinz, Phys. Rev. Lett. **105**, 136805 (2010).
[24] T. Boker, R. Severin, A. Muller, C. Janowitz, R. Manzke, D. Voss, P. Kruger, A. Mazur, and J. Pollmann, Phys. Rev. B **64**, 235305 (2001).
[25] J. K. Ellis, M. J. Lucero, and G. E. Scuseria, Appl. Phys. Lett. **99**, 261908 (2011).
[26] R. Dhall, M. R. Neupane, D. Wickramaratne, M. Mecklenburg, Z. Li, C. Moore, R. K. Lake, and S. Cronin, Adv. Mater. **27**, 1573 (2015).
[27] R. Ganatra and Q. Zhang, ACS Nano **8**, 4074 (2014).
[28] A. Kumar and P. K. Ahluwalia, Eur. Phys. J. B **85**, 186 (2012).
[29] S. B. Desai, G. Seol, J. S. Kang, H. Fang, C. Battaglia, R. Kapadia, J. W. Ager, J. Guo, and A. Javey, Nano Lett. **14**, 4592 (2014).
[30] W. Liu, W. Cao, J. Kang, and K. Banerjee, ECS Trans. **58**, 281 (2013).
[31] R. K. Ghosh and S. Mahapatra, IEEE J. Electron Devices Soc. **1**, 175 (2013).
[32] T. Zandt, H. Dwelk, C. Janowitz, and R. Manzke, J. Alloys Compd. **442**, 216 (2007).
[33] W. G. Dawson and D. W. Bullett, J. Phys. C: Solid State Phys. **20**, 6159 (1987).
[34] Q. H. Yu, Y. Y. Wang, S. Xu, L. L. Sun, and T. L. Xia, EPL. **115**, 37007 (2016).
[35] C. H. Lee, E. Cruz-Silva, L. Calderin, M. A. T. Nguyen, M. J. Hollander, B. Bersch, T. E. Mallouk, and J. A. Robinson, Sci. Rep. **5**, 10013 (2015).
[36] J. Augustin, V. Eyert, T. Boker, W. Frentrup, H. Dwelk, C. Janowitz, and R. Manzke, Phys. Rev. B **62**, 10812 (2000).
[37] B. E. Brown, Acta Crystallogr. **20**, 268 (1966).
[38] A. C. Ferrari and D. M. Basko, Nat. Nanotechnol. **8**, 235 (2013).
[39] G. Abstreiter, E. Bauser, A. Fischer, and K. Ploog, Appl. Phys. **16**, 345 (1978).
[40] X. Zhang, X. F. Qiao, W. Shi, J. B. Wu, D. S. Jiang, and P. H. Tan, Chem. Soc. Rev. **44**, 2757 (2015).
[41] X. Lu, X. Luo, J. Zhang, S. Y. Quek, and Q. H. Xiong, Nano Research **9**, 3559 (2016).
[42] X. Zhang, Q. H. Tan, J. B. Wu, W. Shi, and P. H. Tan, Nanoscale, **8**, 6435 (2016).
[43] K. A. N. Duerloo, Y. Li, and E. J. Reed, Nat. Commun. **5**, 4214 (2014).
[44] K. A. N. Duerloo and E. J. Reed, ACS Nano **10**, 289 (2016).
[45] H. H. Huang, X. F. Fan, D. J. Singh, H. Chen, Q. Jiang, and W. T. Zheng, Phys. Chem. Chem. Phys. **18**, 4086 (2016).
[46] P. E. Blöchl, Phys. Rev. B **50**, 17953 (1994); G. Kresse and D. Joubert, *ibid.* **59**, 1758 (1999).
[47] G. Kresse and J. Hafner, Phys. Rev. B **47**, 558 (1993); G. Kresse and J. Furthmüller, Comput. Mater. Sci. **6**, 15 (1996); Phys. Rev. B **54**, 11169 (1996).
[48] J. P. Perdew, K. Burke, and M. Ernzerhof, Phys. Rev. Lett. **77**, 3865 (1996).
[49] J. Klimeš, D. R. Bowler, and A. Michaelides, Phys. Rev. B **83**, 195131 (2011).
[50] A. Mar, S. Jobic, and J. A. Ibers, J. Am. Chem. Soc. **114**, 8963 (1992).
[51] Q. J. Song, Q. H. Tan, X. Zhang, J. B. Wu, B. W. Sheng, Y. Wan, X. Q. Wang, L. Dai, and P. H. Tan, Phys. Rev. B **93**, 115409 (2016).
[52] H. Guo, T. Yang, M. Yamamoto, L. Zhou, R. Ishikawa, K. Ueno, K. Tsukagoshi, Z. Zhang, M. S. Dresselhaus, and R. Saito, Phys. Rev. B **91**, 205415 (2015).
[53] A. Kokalj, Comp. Mater. Sci. **28**, 155 (2003).